# Broadband infrared plasmonic metamaterial absorber with multipronged absorption mechanisms

CHUN-HAO FANN,[1,3] JIHUA ZHANG,[1,3] MOHAMED ELKABBASH,[1] (iD) WILLIAM R. DONALDSON,[2] E. MICHAEL CAMPBELL,[2] AND CHUNLEI GUO[1,*]

[1]*The Institute of Optics, University of Rochester, Rochester, NY 14627, USA*
[2]*Laboratory for Laser Energetics, University of Rochester, Rochester, NY 14623, USA*
[3]*These authors contribute equally to this work*
[*]*guo@optics.rochester.edu*

**Abstract:** A broadband plasmonic metamaterial absorber with near perfect multiband absorption in the infrared region is designed using a metal-insulator-metal configuration and fabricated using photolithography. The metal-insulator-metal configuration consists of a Ti microdisk array, a $SiO_2$ insulator spacer, and an Al bottom layer. The multiband absorption occurs with near perfect absorption at 4.8–7.5 μm and 9.7–10.5 μm. Ultra-broadband absorption in the mid-IR wavelength range between 3–14 μm is realized by adding a rough photoresist layer on top of the periodic microdisk structures. The multiband absorption is achieved through the combined mechanisms including plasmonic surface lattice resonance, gap plasmon resonance, Fabry-Perot cavity resonance, and the intrinsic phonon-polariton absorption of $SiO_2$.

## 1. Introduction

Plasmonic metamaterial absorbers (PMAs) enable designer light absorption with subwavelength thickness that goes beyond materials' intrinsic absorption [1–3]. The ability to control absorption and thermal radiation is integral to many applications, e.g., photovoltaics, solar energy generation, thermophotovoltaics, thermal imaging, infrared spectroscopy, and sensing [1–7]. For reciprocal materials with symmetric permittivity and permeability tensors, absorptance and emittance of thermal radiation are equivalent according to Kirchhoff's law of thermal radiation [2]. Consequently, PMAs that absorb/emit light strongly within the infrared (IR) enable daytime radiative cooling [8], enhanced photovoltaic cell efficiency [6], radiative cooling based thermoelectric generation [8], and subfreezing passive radiative cooling [2]. Previous PMA designs have been demonstrated using different structures [9–15]. However, a multilayer metal-insulator-metal (MIM) structure is most commonly used due to its thin and simple design [6,16]. The MIM structure usually consists of a top metal layer of periodic nano/micro-structures, a middle insulator spacer layer, and a bottom metal layer acting as a perfect reflector. By designing the MIM structures, different light absorption mechanisms were utilized including: localized electromagnetic dipole resonances [1,17–19], resonant excitation of propagating surface plasmon polariton [20–22], gap plasmon resonances [23–27], localized surface plasmon polariton resonances [28–30], and total internal reflection of the MIM by utilizing 3D nanoparticles [31]. Previous works each mainly relied on a single absorption mechanism to achieve broadband IR absorption e.g., using multi-sized microstructures with different resonance wavelengths [30,32,33], or using stacks of absorber [9,34,35], pyramids [14,19], and asymmetric designs [17,29].

In this paper, a broadband MIM-based PMA is presented with near perfect multiband absorption in the IR. Instead of using multi-sized disks or stacks, the multiband absorption is realized by implementing multiple absorption mechanisms including plasmonic surface lattice resonances,

gap plasmon resonances, Fabry-Perot cavity resonances, and intrinsic material absorption in a single MIM design. By taking advantage of this multiple-mechanism scheme, the absorber is relatively thin, resulting in a simpler fabrication process. Consequently, a near perfect multiband absorption over 90% is realized at 4.8–7.5 µm and 9.7–10.5 µm. An ultra-broadband absorber (3–14 µm) is achieved by using an additional rough photoresist layer of Poly(methyl methacrylate) (PMMA) which creates additional absorption modes and broadens the absorption waveband.

## 2. Design and simulation

The MIM design, shown in Fig. 1, consists of a top layer of titanium (Ti) microdisk array, a spacer layer of $SiO_2$, and a bottom layer of aluminum (Al) on a glass substrate. Unlike previous designs using Au [36] or Ag [37] as the top metal layer, Ti is used due to its higher optical losses in the IR, corrosion resistance, and wide spread use in industry. The Ti microdisks are 30 nm thick with a period and diameter denoted as $P$ and $d$, respectively. $SiO_2$ is used as the insulator layer due to its intrinsic phonon-polariton absorption in the IR with its thickness defined as $t$. Al is used as the bottom layer due to its reflective property as a near perfect electric conductor in the IR and its availability in industry. Al thickness is designed to be 100 nm to ensure zero transmission in the IR.
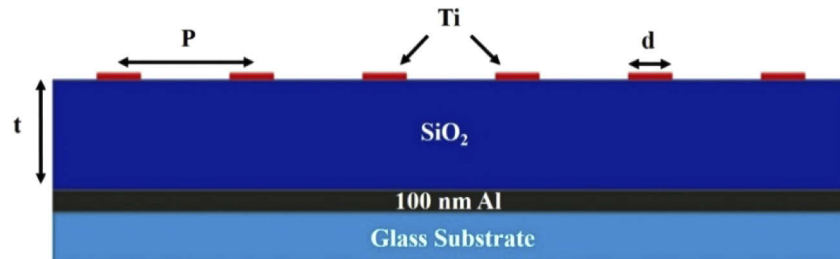


**Fig. 1.** Schematic of the cross-section view of the proposed MIM-based PMA design.

Finite-difference time-domain simulations were performed to calculate the absorption spectra of the designed PMA. Figure 2(a) shows the absorption spectrum of the optimized final design with $P = 4$ µm, $d = 2$ µm, and $t = 1$ µm. The PMA supports multiband absorption in the IR. There are eight absorption bands with peaks at 4.18 µm, 4.55 µm, 5.64 µm, 6.74 µm, 8.38 µm, 10.01 µm, 10.87 µm, and 12.66 µm, which correspond to different absorption mechanisms. We label them from A-I to A-VIII, with colors based on their absorption mechanisms namely; plasmonic surface lattice resonances in red, Fabry-Perot cavity resonances in navy blue, gap plasmon resonances in orange, and intrinsic material absorption of $SiO_2$ in olive-green. To distinguish between the different absorption mechanisms, we calculated the absorption for each component of the PMA separately. Figure 2(b) shows the absorption contribution of each component of the PMA, i.e., the power dissipated inside each component. Figure 2(c) shows the absorption of a 100 nm Al on glass, 1000 nm $SiO_2$ on 100 nm Al on glass, and Ti microdisk array on glass. Finally, the absorption of the PMA as a function of $t$, $P$, and $d$ are shown in Figs. 2(d)–2(f), respectively, while holding all other parameters unchanged.

Figure 2(b) shows that most of the absorption corresponding to A-I, A-II, A-III, A-IV, and A-VII occurs inside the Ti microdisk layer (blue line), while the absorption corresponding to A-V, A-VI, A-VII occurs inside the $SiO_2$ layer (red line). The Al layer has limited contribution to absorption in the studied wavelength region (green line). A minor absorption peak near A-II is observed in both the $SiO_2$ and Al indicating that this peak is due to a Fabry-Perot cavity resonance which naturally leads to absorption in both the metal and dielectric films if the dielectric has non-zero extinction coefficient [38].
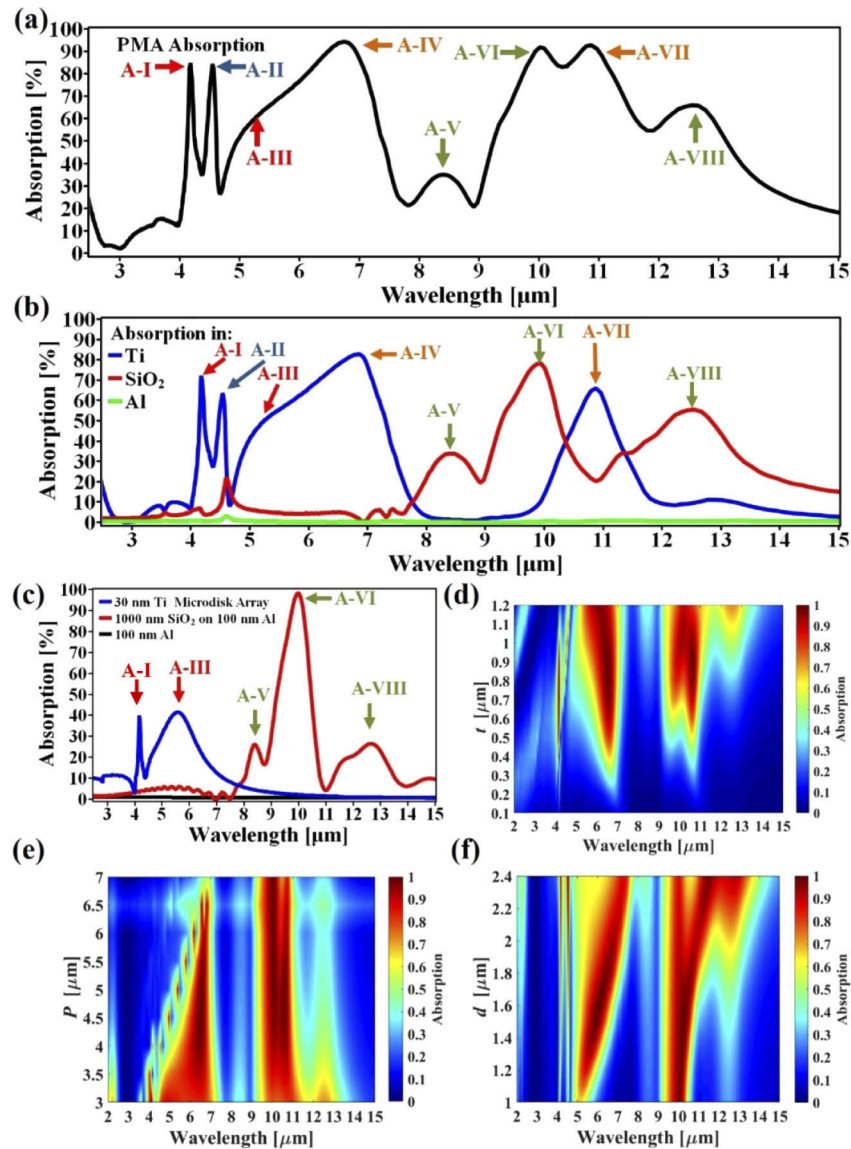
**Fig. 2.** (a) Simulated absorption spectrum of the final PMA design with $d = 2$ μm $P = 4$ μm, and $t = 1$ μm. There are eight absorption peaks which are labeled as A-I to A-VIII with colors based on their absorption mechanisms; plasmonic surface lattice resonances in red, Fabry-Perot cavity resonances in navy blue, gap plasmon resonances in orange, and the $SiO_2$ intrinsic material absorption in olive-green. (b) Absorption contributions from each material in the final PMA. (c) Absorption spectra of 30 nm Ti microdisk array on glass (black), 1 μm $SiO_2$ on 100 nm Al (blue), and 100 nm Al (red). (d) Absorption spectra as a function of $t$ with fixed $d = 2$ μm and $P = 4$ μm. (e) Absorption spectra as a function of $P$ with fixed $d = 2$ μm and $t = 1$ μm. (f) Absorption spectra as a function of $d$ with fixed $P = 4$ μm and $t = 1$ μm.

Figure 2(c) shows the absorptance of each element separately which allows us to recognize absorption mechanisms that does not require synergy between the different elements of our PMA. The absorption peaks A-I (4.18 μm) and A-III (5.64 μm) exist in the isolated 30nm-thick Ti microdisks array (blue line) arise due to plasmonic surface lattice resonances [39], which occurs when the array period is comparable to the wavelength so that first-order diffraction of the periodic structure is in the plane of the array and strongly couples with the localized surface plasmon polaritons in each microdisk. Among them, A-I and A-III correspond to the diffraction in air and in the SiO$_2$, respectively. Both plasmonic surface lattice resonances belong to the first type, which occurs at a wavelength slightly longer than the diffraction edge of $nP$ for normal incidence where $n$ is the refractive index of air or SiO$_2$ [39]. The absorption spectrum of the 1000 nm SiO$_2$ on Al (red line) shows a main peak near A-VI (10.01 μm) and two minor peaks at A-V (8.38 μm) and A-VIII (12.66 μm), due to the intrinsic phonon-polariton absorption of the SiO$_2$ layer. On the other hand, the absorption bands A-IV and A-VII are not present in Fig. 2(c), i.e., these resonances are only supported in the MIM structures, indicating that they are due to the excitation of the gap plasmon resonance.

Figure 2(d) shows the calculated absorption as a function of $t$. We note that the spectral location of A-V (8.38 μm), A-VI (10.01 μm) and A-VIII (12.66 μm) are independent of $t$ which confirms that they appear due to the intrinsic absorption of SiO$_2$. On the other hand, A-II (4.55 μm) spectral position redshifts when increasing $t$. For a dielectric-metal stack the maximum absorption wavelength $\lambda_{\mathrm{max}}$ is given by [38]

$$\lambda_{\mathrm{max}} = 2\pi n_d t \tan\left(n_d \sqrt{\frac{n_m - n_0}{n_0(n_d^2 - n_m n_0)}}\right), \tag{1}$$

where $n_{\mathrm{d}}$ is the dielectric refractive index, $n_{\mathrm{m}}$ is the metallic substrate refractive index, $n_0$ is the superstrate refractive index. Accordingly, the red shift in $\lambda_{\mathrm{max}}$ as a function of $t$ confirms that A-II absorption band is due to Fabry-Perot cavity resonance mechanism.

Figure 2(e) shows the calculated absorption as a function of $P$. Changing $P$ mainly affects the location of A-I and A-III, i.e., the absorption due to plasmonic surface lattice resonance. As $P$ increases, we see that A-I and A-III $\lambda_{\mathrm{max}}$ redshifts, and the absorption-line narrows. These observations agree with the results obtained previously by Zou *et. al.* on plasmonic surface lattice resonance [40,41]. Hence, to maximize the absorption bandwidth based on plasmonic surface lattice resonance, decreasing the period is necessary. It is interesting to note that the concept of super-radiance applied to plasmonic nanoantenna arrays predicts a similar behavior, i.e., that for closely packed plasmonic antennas, the bandwidth of the collective excitation is inversely proportional to $P$ [42] due to the enhanced radiation efficiency of the antennas which leads to reduced quality factor [43].

Finally, in Fig. 2(f) we observe a redshift in A-IV and A-VII that only appear for the MIM structure due to gap plasmon resonance. This is because a gap plasmon resonance occurs due to Fabry-Perot excitations through multiple reflections at the edges of the MIM structures, here delineated by the top Ti disk. For gap plasmon resonance [44],

$$\lambda_{\mathrm{max}} = d n_{GSP}\left(\frac{2\pi}{m\pi - \varphi}\right), \tag{2}$$

where $n_{\mathrm{GSP}}$ is the real part of the effective mode index of the gap surface plasmon, $m$ is an integer defining the order of the gap surface plasmon mode, and $\varphi$ s an additional phase shift acquired upon reflection at the boundaries of the MIM configuration. Consequently, as we increase the nanoparticle $d$, $\lambda_{\mathrm{max}}$ redshifts. We note here that increasing the absorptance of gap plasmon resonant mode depends on the spacer thickness (i.e., $t$) as is evident in Fig. 2(d).

## 3. Experimental demonstration

The PMA is fabricated and characterized based on the simulated design. Figure 3(a) depicts the fabrication procedure in seven steps. First, a glass substrate is prepared and cleaned. Second, a layer of Al with thickness of 100 nm is deposited using electron beam evaporation. Third, a layer of $SiO_2$ with thickness of 1000 nm is deposited onto the Al layer. Then, the sample is spin coated with a photoresist layer of PMMA. After that, photolithography is used to define the circular microdisk array on the PMMA. Next, Ti with thickness of 30 nm is deposited using electron beam evaporation. Finally, the PMMA photoresist and unwanted Ti are removed using lift-off process. Figures 3(b) and 3(c) show the optical image of the fabricated sample and the scanning electron microscope (SEM) image of the microdisks, respectively. It is found that the resulting microdisks are uniform in period $P = 4 \mu m$ and size $d = 2 \mu m$.
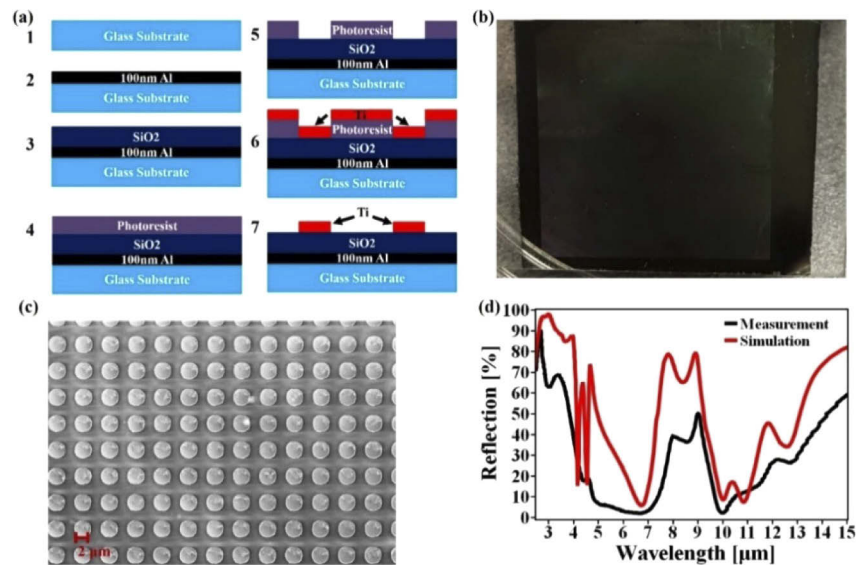


**Fig. 3.** (a) Schematic showing the seven steps of the fabrication procedure of the PMA. (b) Image of the fabricated sample. (c) SEM image of the microdisks. (d) Experimental measurement and theoretical simulation of the reflection spectra for the PMA.

The total reflection of the sample is measured using a Fourier-transform IR Spectrometer with an integrating sphere accessory. Figure 3(d) shows the measured result (black line) which is broader and more absorptive than the simulation (red line), particularly for A-III. In experiment, the absorption is larger than 80% in two broadbands at 4.3–7.65 μm and 9.5–11.7 μm, and larger than 90% at 4.8–7.5 μm and 9.7–10.5 μm. The absorption is broadened by combining the absorption peaks from A-I to A-IV. The broader absorption in experiment is likely due to the surface roughness of the top layer Ti microdisks, resulting in a much stronger absorption due to inducing localized plasmons [45] (see Fig. 6).

The angular dependence of the multiband absorption is also studied, as shown in Fig. 4. The specular reflectance with different incident angles defined as $\theta$ is also measured from 2.5 μm to 16 μm. The results are measured for $\theta = 10°$ to $\theta = 70°$ with 20° intervals. It is shown that the absorption in broadband remains strong for incident angle $\theta < 50°$. This result indicates that the effect of the incidence angle is minimal for the PMA for angles below $\theta = 50°$. A strong angular dependence is present for incident angles $\theta > 50°$, which significantly increases for $\theta > 70°$. There is a blue shift of A-I and A-III due to the shift of phase matching wavelength for

surface first-order diffraction. The position of other absorption peaks remain mostly constant for all incident angles.
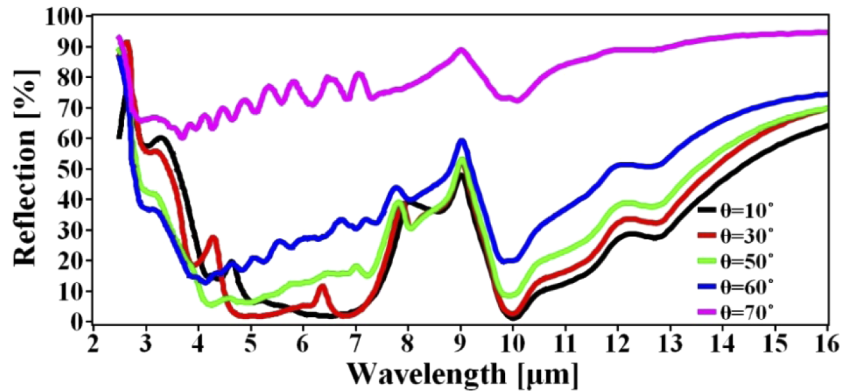


**Fig. 4.** Measured specular reflection of the multiband PMA at incident angles of $\theta = 10°$ to $\theta = 70°$ with 20° intervals.

Finally, broader absorption is achieved by leaving some PMMA photoresist on top of the PMA sample. This is realized by controlling the time of removing the PMMA resist in the lift-off process. The sample is taken out from the resist removal solution before the resist is fully dissolved. As a result, a layer of rough PMMA with random thickness is left on top of the PMA, which helps to broaden the absorption. Another mechanism lies in that PMMA is known to have intrinsic absorption at 5 μm - 10 μm. The specular reflectance is measured from 2.5 μm to 25 μm for $\theta = 10°$ to $\theta = 70°$ with 20° intervals as shown in Fig. 5, showing enhanced overall absorption when adding rough PMMA. Compared to Fig. 4, the absorption peaks from A-I to A-VIII are still observable in Fig. 5. However, the absorption modes overlap over the entire range from 3 μm −14 μm. The broadband dependence of $\theta$ is similar to the PMA without PMMA where it is minimal for angle below $\theta = 50°$. The observed redshift is independent of the incident angle [25]. Due to this change in refractive index, the PMA can be further broadened [22]. Another advantage of the PMMA coating is to further protect the microdisk structures from physical abrasions and damage.
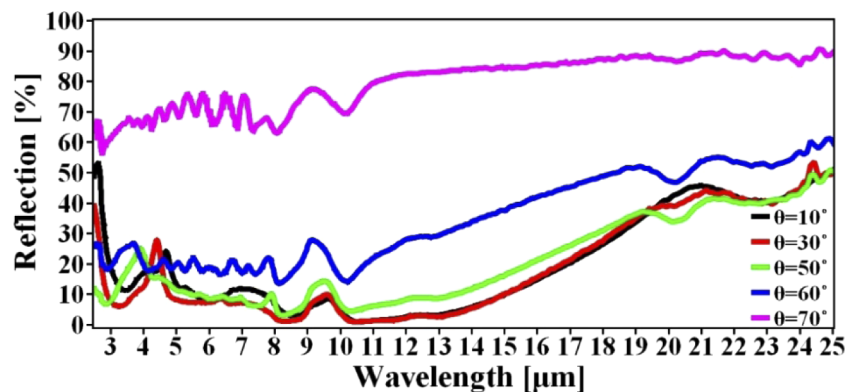


**Fig. 5.** Measured specular reflection of the PMA with a thin photoresist layer of PMMA.

Broadband absorption in the IR region have been studied recently using transparent conductive oxides as top plasmonic materials [46,47]. Although these studies also used a three-layer design,

the patterned top absorbing materials are very different from our design. Furthermore, the mechanisms of the broadband IR absorption and the structural dimension of those studies are also different from ours. In Ref. [46], the authors used Al-doped ZnO as the top absorbing material, which has broadband absorption in the IR. The broadband absorption was further enhanced by patterning the Al-doped ZnO film into a square array with a high filling factor. In Ref. [47], the broadband IR absorption depended on using disordered, densely packed, and tilted ITO nanorod forests as the top absorbing layer. In contrast, the broadband IR absorption in our work is based on the excitation of multipronged absorption mechanisms, which makes our design having more controllability on the absorption. For instance, it can be designed to realize selective absorption as well by tuning the absorption wavelengths of each mechanism. In addition, the absorption is further broadened by adding a rough PMMA layer. The top Ti microdisks are relatively large in size and gap, they can be fabricated by photolithography.

## 4. Conclusion

In conclusion, by utilizing combined mechanisms including plasmonic surface lattice resonance, Fabry-Perot cavity resonance, gap plasmon resonance, and intrinsic material absorption, a near perfect multiband MIM-based PMA covering the atmospheric windows in the IR region is achieved. This allows the absorber to be thinner and simpler for fabrication. Furthermore, an ultra-broadband absorption from 3 μm to 14 μm is achieved by adding an additional photoresist layer of PMMA, enhancing and broadening the absorption. This work may lead to further improvements in various practical applications ranging from sensing, controlled thermal radiation, thermophotovoltaics, and spectrometry.

## Appendix
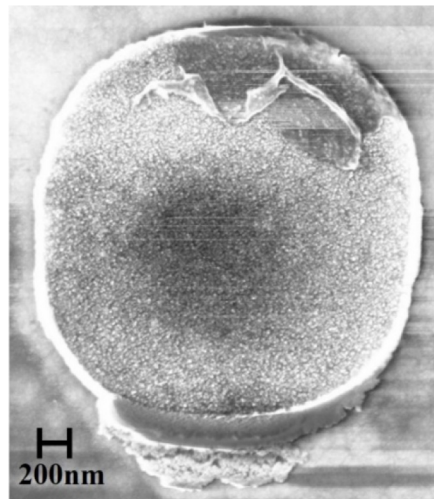


**Fig. 6.** SEM image of one of the Ti Microdisks. The surface is quite rough as noted by the tiny white dots on the disk as well as some remaining photoresist on the top.

## Acknowledgments

## Disclosures

The authors declare no conflicts of interest.

## References

1. X. Liu, T. Starr, A. F. Starr, and W. J. Padilla, "Infrared spatial and frequency selective metamaterial with near-unity absorbance," Phys. Rev. Lett. **104**(20), 207403 (2010).
2. Y. Cui, Y. He, Y. Jin, F. Ding, L. Yang, Y. Ye, S. Zhong, Y. Lin, and S. He, "Plasmonic and metamaterial structures as electromagnetic absorbers," Laser Photonics Rev. **8**(4), 495–520 (2014).
3. C. M. Watts, X. Liu, and W. J. Padilla, "Metamaterial electromagnetic wave absorbers," Adv. Mater. **24**(23), OP98–OP120 (2012).
4. Y. Ra'di, C. R. Simovski, and S. A. Tretyakov, "Thin perfect absorbers for electromagnetic waves: theory, design, and realizations," Phys. Rev. A **3**(3), 037001 (2015).
5. T. D. Dao, K. Chen, S. Ishii, A. Ohi, T. Nabatame, M. Kitajima, and T. Nagao, "Infrared perfect absorbers fabricated by colloidal mask etching of Al–Al2O3–Al trilayers," ACS Photonics **2**(7), 964–970 (2015).
6. S. Ogawa and M. Kimata, "Metal-insulator-metal-based plasmonic metamaterial absorbers at visible and infrared wavelengths: a review," Materials **11**(3), 458 (2018).
7. C. Wu, B. Neuner III, J. John, A. Milder, B Zollars, S. Savoy, and G. Shvets, "Metamaterial-based integrated plasmonic absorber/emitter for solar thermo-photovoltaic systems," J. Opt. **14**(2), 024005 (2012).
8. B. Ko, D. Lee, T. Badloe, and J. Rho, "Metamaterial-Based Radiative Cooling: Towards Energy-Free All-Day Cooling," Energies **12**(1), 89 (2018).
9. Y. Q. Ye, Y. Jin, and S. He, "Ominidirectional, polarization-insensitive and broadband thin absorber in the terahertz regime," J. Opt. Soc. Am. B **27**(3), 498–504 (2010).
10. M. A. Kats, R. Blanchard, P. Genevet, and F. Capasso, "Nanometre optical coatings based on strong interference effects in highly absorbing media," Nat. Mater. **12**(1), 20–24 (2013).
11. B. Wang, T. Koschny, and C. M. Soukoulis, ""Wide-angle and polarization-independent chiral metamaterial absorber," Phys. Rev. B **80**(3), 033108 (2009).
12. Y. Cui, K. H. Fung, J. Xu, H. Ma, Y. Jin, S. He, and N. X. Fang, "Ultrabroadband light absorption by a sawtooth anisotropic metamaterial slab," Nano Lett. **12**(3), 1443–1447 (2012).
13. Y.-K. R. Wu, A. E. Hollowell, C. Zhang, and L. J. Guo, "Angle-insensitive structural colours based on metallic nanocavities and coloured pixels beyond the diffraction limit," Sci. Rep. **3**(1), 1194 (2013).
14. J. Zhu, Z. Ma, W. Sun, F. Ding, Q. He, L. Zhou, and Y. Ma, "Ultra-broadband terahertz metamaterial absorber," Appl. Phys. Lett. **105**(2), 021102 (2014).
15. Y. Cui, K. H. Fung, J. Xu, S. He, and N. X. Fang, "Multiband plasmonic absorber based on transverse phase resonances," Opt. Express **20**(16), 17552–17559 (2012).
16. N. I. Landy, C. M. Bingham, T. Tyler, N. Jokerst, D. R. Smith, and W. J. Padilla, "Design, theory, and measurement of a polarization-insensitive absorber for terahertz imaging," Phys. Rev. B **79**(12), 125104 (2009).
17. B. Zhang, Y. Zhao, Q. Hao, B. Kiraly, I.-C. Khoo, S. Chen, and T. J. Huang, "Polarization-independent dual-band infrared perfect absorber based on a metal-dielectric-metal elliptical nanodisk array," Opt. Express **19**(16), 15221–15228 (2011).
18. K. B. Alici, A. B. Turhan, C. M. Soukoulis, and E. Ozbay, "Optically thin composite resonant absorber at the near-infrared band: A polarization independent and spectrally broadband configuration," Opt. Express **19**(15), 14260–14267 (2011).
19. J. Hao, J. Wang, X. Liu, W. J. Padilla, L. Zhou, and M. Qiu, "High performance optical absorber based on a plasmonic metamaterial," Appl. Phys. Lett. **96**(25), 251104 (2010).
20. P. Chevalier, P. Bouchon, J. Jaeck, D. Lauwick, N. Bardou, A. Kattnig, F. Pardo, and R. Haïdar, "Absorbing metasurface created by diffractionless disordered arrays of nanoantennas," Appl. Phys. Lett. **107**(25), 251108 (2015).
21. L. Lin and Y. Zheng, "Optimizing plasmonic nanoantennas via coordinated multiple coupling," Sci. Rep. **5**(1), 14788 (2015).
22. K. Chen, R. Adato, and H. Altug, "Dual-band perfect absorber for multispectral plasmon-enhanced infrared spectroscopy," ACS Nano **6**(9), 7998–8006 (2012).
23. M. G. Nielsen, D. K. Gramotnev, A. Pors, O. Albrektsen, and S. I. Bozhevolnyi, "Continuous layer gap plasmon resonators," Opt. Express **19**(20), 19310–19322 (2011).
24. A. Pors, O. Albrektsen, I. P. Radko, and S. I. Bozhevolnyi, "Gap plasmon-based metasurfaces for total control of reflected light," Sci. Rep. **3**(1), 2155 (2013).
25. J. S. Clausen, E. Højlund-Nielsen, A. B. Christiansen, S. Yazdi, M. Grajower, H. Taha, U. Levy, A. Kristensen, and N. A. Mortensen, "Plasmonic Metasurfaces for Coloration of Plastic Consumer Products," Nano Lett. **14**(8), 4499–4504 (2014).

26. Z. Li, E. Palacios, S. Butun, and K. Aydin, "Visible-frequency metasurfaces for broadband anomalous reflection and high-efficiency spectrum splitting," Nano Lett. **15**(3), 1615–1621 (2015).

27. S.-C. Jiang, X. Xiong, Y.-S. Hu, S.-W. Jiang, Y.-H. Hu, D.-H. Xu, R.-W. Peng, and M. Wang, "High-efficiency generation of circularly polarized light via symmetry-induced anomalous reflection," Phys. Rev. B **91**(12), 125421 (2015).

28. K. Aydin, V. E. Ferry, R. M. Briggs, and H. A. Atwater, "Broadband polarization independent resonant light absorption using ultrathin plasmonic super absorbers," Nat. Commun. **2**(1), 517 (2011).

29. M. K. Hedayati, M. Javaherirahim, B. Mozooni, R. Abdelaziz, A. Tavassolizadeh, V. S. K. Chakravadhanula, V. Zaporojtchenko, T. Strunkus, F. Faupel, and M. Elbahri, "Design of a perfect black absorber at visible frequencies using plasmonic metamaterials," Adv. Mater. **23**(45), 5410–5414 (2011).

30. C.-W. Cheng, M. N. Abbas, C.-W. Chiu, K.-T. Lai, M.-H. Shih, and Y.-C. Chang, "Wide-angle polarization independent infrared broadband absorbers based on metallic multi-sized disk arrays," Opt. Express **20**(9), 10376–10381 (2012).

31. V. G. Kravets, S. Neubeck, and A. N. Grigorenko, "Plasmonic blackbody: Strong absorption of light by metal nanoparticles embedded in a dielectric matrix," Phys. Rev. B **81**(16), 165401 (2010).

32. B. Zhang, J. Hendrickson, and J. Guo, "Multispectral near-perfect metamaterial absorbers using spatially multiplexed plasmon resonance metal square structures," J. Opt. Soc. Am. B **30**(3), 656–662 (2013).

33. X. Liu, T. Tyler, T. Starr, A. F. Starr, N. M. Jokerst, and W. J. Padilla, "Taming the blackbody with infrared metamaterials as selective thermal emitters," Phys. Rev. Lett. **107**(4), 045901 (2011).

34. G. Kenanakis, C. P. Mavidis, E. Vasilaki, N. Katsarakis, M. Kafesaki, E. N. Economou, and C. M. Soukoulis, "Perfect absorbers based on metal-insulator-metal structures in the visible region: a simple approach for practical applications," Appl. Phys. A **123**(1), 77 (2017).

35. J. Wang, C. Fan, P. Ding, J. He, Y. Cheng, W. Hu, G. Cai, E. Liang, and Q. Xue, "Tunable broad-band perfect absorber by exciting of multiple plasmon resonances at optical frequency," Opt. Express **20**(14), 14871–14878 (2012).

36. A. A. Jamali and B. Witzigmann, "Plasmonic Perfect Absorbers for Biosensing Applications," Plasmonics **9**(6), 1265–1270 (2014).

37. W. L. Barnes, A. Dereux, and T. W. Ebbesen, "Surface plasmon subwavelength optics," Nature **424**(6950), 824–830 (2003).

38. M. ElKabbash, S. Iram, T. Letsou, M. Hinczewski, and G. Strangi, "Designer Perfect Light Absorption Using Ultrathin Lossless Dielectrics on Absorptive Substrates," Adv. Opt. Mater. **6**(22), 1800672 (2018).

39. V. G. Kravets, A. V. Kabashin, W. L. Barnes, and A. N. Grigorenko, "Plasmonic Surface Lattice Resonances: A Review of Properties and Applications," Chem. Rev. **118**(12), 5912–5951 (2018).

40. S. L. Zou, N. Janel, and G. C. Schatz, "Silver nanoparticle array structures that produce remarkably narrow plasmon lineshapes," J. Chem. Phys. **120**(23), 10871–10875 (2004).

41. V. A. Markel, "Comment on "Silver nanoparticle array structures that produce remarkably narrow plasmon lineshapes"," J. Chem. Phys. **122**(9), 097101 (2005).

42. S. Choudhary, S. D. Swiecicki, I. De Leon, S. A. Schulz, J. Upham, J. E. Sipe, and R. W. Boyd, "Superradiance in arrays of plasmonic nanoantennas," *Frontiers in Optics 2016*, FTu3D (2016).

43. M. S. Eggleston, K. Messer, L. Zhang, E. Yablonovitch, and M. C. Wu, "Optical antenna enhanced spontaneous emission," Proc. Natl. Acad. Sci. **112**(6), 1704–1709 (2015).

44. F. Ding, Y. Yang, A. Deshpande Rucha, and I. Bozhevolnyi Sergey, "A review of gap-surface plasmon metasurfaces: fundamentals and applications," Nanophotonics **7**(6), 1129–1156 (2018).

45. K. M. Byun, S. J. Yoon, and D. Kim, "Effect of surface roughness on the extinction-based localized surface plasmon resonance biosensors," **Appl. Opt.** **47**(31), 5886–5892 (2008).

46. K. Sun, C. A. Riedel, Y. D. Wang, A. Urbani, M. Simeoni, S. Mengali, M. Zalkovskij, B. Bilenberg, C. H. de Groot, and O. L. Muskens, "Metasurface Optical Solar Reflectors Using AZO Transparent Conducting Oxides for Radiative Cooling of Spacecraft," ACS Photonics **5**(2), 495–501 (2018).

47. D. U. Yildirim, A. Ghobadi, M. C. Soydan, O. Atesal, A. Toprak, M. D. Caliskan, and E. Ozbay, "Disordered and Densely Packed ITO Nanorods as an Excellent Lithography-Free Optical Solar Reflector Metasurface," ACS Photonics **6**(7), 1812–1822 (2019).